

<https://doi.org/10.1038/s41612-026-01327-6>

Accelerated reduction of atmospheric ultrafine particles since China VI vehicle emission standards

Check for updates

Haoqian Wang^{1,13}, Yifan Wen^{2,13}, Jin Wu³, Runlong Cai⁴, Yicheng Shen⁵, Chenjuan Deng³, Yuyang Li³, Yiran Li³, Hao Wu³, Dandan Huang⁶, Hairong Cheng¹, Chao Yan⁷, Jian Gao⁵, Mei Zheng⁸, Yongchun Liu⁹, Markku Kulmala^{9,10}, Feiyue Mao¹¹, James N. Smith¹², Shaojun Zhang³, Jiming Hao³, Xiaoxiao Li^{1,6} ✉ & Jingkun Jiang³ ✉

Vehicle emission is a major source of urban ultrafine particles (UFPs), yet measurement and emission control for UFP lags significantly behind that of other pollutants. The China VI emission standard, one of the strictest globally, introduced the nation's first particle number (PN) limits. This study focused on real-world PN emissions in the capital city Beijing, which adopted China VI ahead of the national schedule in 2019. Based on long-term particle number size distribution measurements and online UFP composition analysis, a pronounced decline in emission rates of vehicle-attributed PN from 2019 to 2023 was found, resulting in decreases of ~70% for atmospheric $PN_{3-30\text{ nm}}$, ~48% for $PN_{30-100\text{ nm}}$, and ~42% for $PN_{>100\text{ nm}}$. These reductions substantially outpace those observed for $PM_{2.5}$ and NO_2 . Early implementation of China VI, coupled with rapid electric vehicle adoption, are the primary drivers behind Beijing's more pronounced PN mitigation (−44%) compared with nationwide (−33%). These findings highlight the effectiveness of more stringent vehicle emission standards and electric vehicle strategies in reducing atmospheric UFPs, shedding light on future vehicle emission regulations.

Ultrafine particles (UFPs, particle diameters <100 nm) profoundly impact climate and human health by influencing cloud formation and penetrating deep into the pulmonary and circulatory systems^{1,2}. Despite the World Health Organization's call for UFP monitoring³, their sources remain highly complex and uncertain, particularly in rapidly urbanizing regions. Vehicles are one of the major primary sources of UFPs in urban areas^{4,5}. They comprise both solid particle numbers (PN) from direct emission and volatile PN from nucleation of volatile compounds in exhaust^{6,7}. The contribution of vehicle emissions to atmospheric UFPs is highly spatiotemporally variable⁸⁻¹⁰, particularly in the sub-30 nm ranges that dominate near-roadway environments^{11,12}, while attenuating quickly within 100–300 m¹³⁻¹⁵. The high spatiotemporally variability complicate accurate source attribution—a prerequisite for effective regulation.

China has experienced explosive increases in vehicle population, which increased from 15 million in 2000 to 352 million in 2024^{16,17}. Meanwhile, increasingly stringent emission standards have been implemented to mitigate vehicle emissions. The latest China VI standard was implemented in Beijing in 2019, subsequently rolled out to other Chinese regions in 2021. China VI firstly introduced emission limits for solid PN¹⁸, driving adoption of particulate filters (DPF/GPF) and more efficient hydrocarbon (HC)

control equipment¹⁹⁻²¹. On-road tests showed that the UFP emission factor of diesel trucks reduced by 93% from China III to China VI²¹. Meanwhile, the promotion of electric vehicles theoretically promises a substantial reduction of pollutants^{22,23}. However, the real-world effectiveness of new strategies in reducing atmospheric UFPs remains unverified^{24,25}, due to potential aftertreatment tampering²⁵ and slow fleet turnover.

Europe and the US began implementing vehicle emission control at an earlier stage, providing a reference for evaluating the impact of relevant policies on atmospheric UFPs in China. Europe has taken the lead in incorporating solid PN into emission standards: implemented for light-duty diesel vehicles in 2011 (Euro 5b) and extended to all direct injection light-duty vehicles in 2014 (Euro 6)²⁶. Furthermore, some long-term UFP monitoring networks have been established in Europe. The German Ultrafine Aerosol Network (GUAN, including 16 sites) observed a decline rate of 1.7–17.2% year⁻¹ for 10–30 nm PN between 2009 and 2018²⁷. The RI-URBANS (including 20 sites across Europe and 1 site in the US) showed 5.13% annual decline in total PN and 4.50% annual decline in UFPs at traffic sites²⁸. The US has not yet directly incorporated PN into its vehicle emission standards. However, with the increasingly stringent

A full list of affiliations appears at the end of the paper. ✉ e-mail: lixiaoxiao@whu.edu.cn; jiangjk@tsinghua.edu.cn

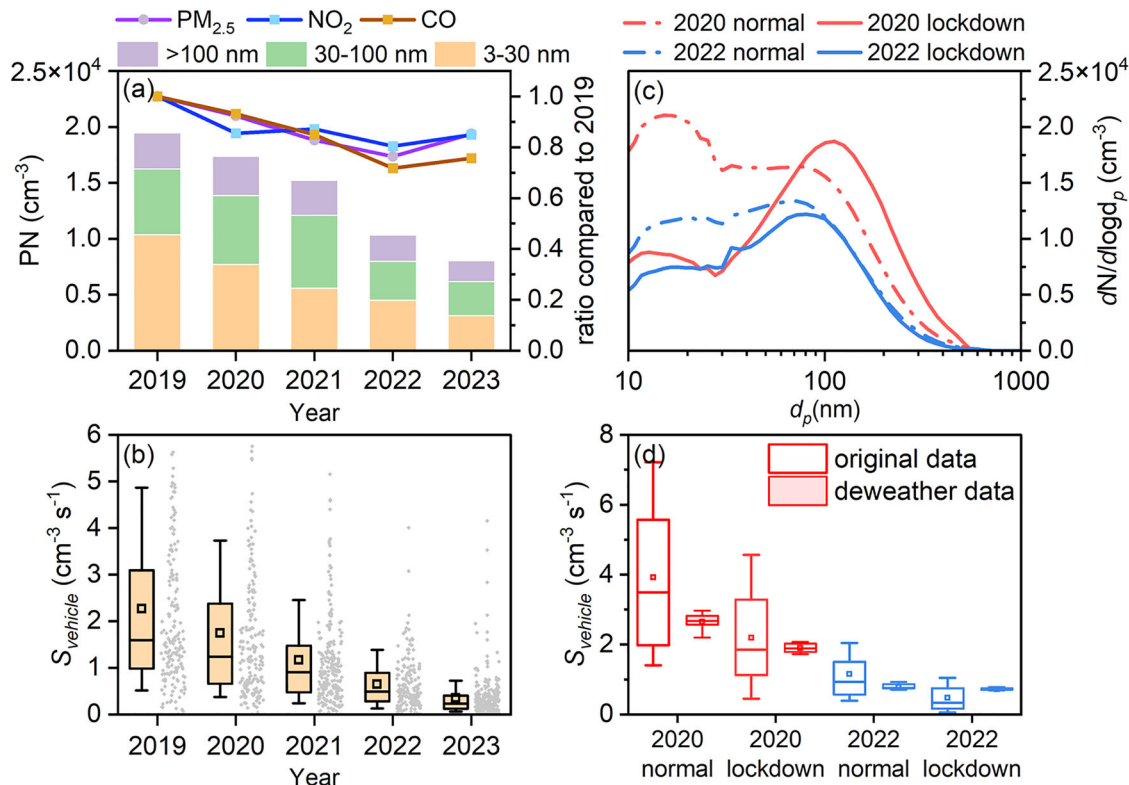


Fig. 1 | Variations in atmospheric PN and vehicle-attributed UFP emission rates (S_{vehicle}) from 2019 to 2023 and during short-term lockdowns. Annual averaged PN, $\text{PM}_{2.5}$, NO_2 and CO (a) and S_{vehicle} (b) in morning rush hours. Average particle size distribution (c) and S_{vehicle} before and after meteorological normalization (d) between lockdown and normal days in winter. 2020 COVID-19 lockdown period

was from Jan. 24th to Feb 29th, 2022 Winter Olympics lockdown period was from Jan. 31st to Feb. 20th. Boxes represent the 25th and 75th values, the length of the whiskers represents 10th and 90th values, the line in the box is the median value and the square represents the mean value.

Tier II (2004) and Tier III (2014) standards, UFPs have decreased by 30% from 2006 to 2016 at 11 observation sites²⁹.

Long-term observation networks and regular emission inventories for atmospheric PN attributed to vehicles have not been established in China. In specific, source attribution of atmospheric UFPs has lagged behind the larger particles (e.g., $\text{PM}_{2.5}$ and PM_1), due to the lack of online measurements of UFP chemical compositions. Previous studies have applied the mode-fitting or positive matrix factorization (PMF) method to particle number size distribution (PNSD), which found Aitken mode particles (20–90 nm³⁰) are highly related to traffic emissions^{31–33}. However, existing PMF studies either rely solely on PNSD characteristics of different sources for separation, lack of chemical evidence, or utilize offline-sampled chemical composition data with time resolution as high as several hours, making it difficult to capture rapid and intense variations in emission sources (e.g., vehicle and cooking activities)^{34–36}. Simultaneous measurement of UFP composition would help separate vehicle-attributed UFPs more accurately. Alternatively, the aerosol general dynamic equation can quantify PN attributed to primary emissions more accurately, with the consideration of condensation growth and coagulation loss³⁷.

In this study, we quantified the temporal variations of vehicle-attributed UFPs in urban Beijing based on a long-term field observation and explored the driver of the temporal trend based on the emission inventory tool. We applied a home-built thermal desorption chemical ionization mass spectrometer (TDCIMS)³⁸ to semi-continuously measure the chemical composition of UFPs down to 10 nm. Together with continuous PNSD observation and dynamic calculation at multiple urban sites, we extracted emission rates of vehicle-attributed UFPs from 2019 to 2023, as well as their reduction during the COVID-19 lockdown period and the 2022 Winter Olympics. The observation showed significant decrease of UFPs, especially for sub-30 nm particles. The emission inventory analysis revealed the higher

reduction of PN in Beijing than in other parts of China, highlighting the effectiveness of PN emission standards.

Results

Long-term decrease of vehicle-attributed UFPs in urban Beijing

The annual variations of atmospheric PN at the BUCT observation site (on the campus of Beijing University of Chemical Technology, see section “Field sampling and quantification”) are shown in Fig. 1. The total PN decreased from $(1.94 \pm 0.66) \times 10^4 \text{ cm}^{-3}$ in 2019 to $(0.82 \pm 0.27) \times 10^4 \text{ cm}^{-3}$ in 2023, with a decreasing ratio of ~58% (Fig. 1a). Meanwhile, the annual average NO_2 and $\text{PM}_{2.5}$ reduced by ~15% and CO reduced by ~25%, as CO is acknowledged a better indicator in primary combustion emissions than NO_2 and $\text{PM}_{2.5}$. The decrease in CO, NO_2 and $\text{PM}_{2.5}$ was all significantly smaller than PN, indicating an accelerated reduction in atmospheric PN. What’s more, PN at 3–30 nm (PN_{3-30}) decreased from $(1.03 \pm 0.61) \times 10^4 \text{ cm}^{-3}$ in 2019 to $(0.31 \pm 0.15) \times 10^4 \text{ cm}^{-3}$ in 2023, with a decreasing ratio of ~70%, while PN_{30-100} and $\text{PN}_{>100}$ decreased by ~48% and ~42%, respectively. This indicated that the decrease of particles with smaller sizes is more significant than the decrease of larger sizes.

Reduction of nucleation mode particles has been reported in some regions in Europe and the US, but generally with a slighter decreasing level. Observations spanning more than five years across 15 European cities and one U.S. city indicate that PNC reduced by 5.13% annually at traffic sites, while it reduced by 1.89% at urban background sites²⁸. Observations from 11 sites across North America indicate that atmospheric UFPs decreased by ~30% from 2006 to 2016. Near-road PN declined by an order of magnitude from 2001 to 2007, while significant spatial variations exist among different cities²⁹.

Otherwise, some studies in Europe reported inefficient response of nucleation mode particles to vehicle control strategies (e.g., Budapest²⁸ and

London³⁹), possibly due to the ineffectiveness in removing organic vapors, which are the main source of vehicle-attributed nucleation particles. The significant decrease in nucleation mode particles in Beijing is attributed to both the new limit for PN and the stricter limit for organic vapor emissions under China VI standards. For light duty gasoline vehicles (LDGVs), the total hydrocarbon (THC) and non-methane hydrocarbon (NMHC) limits under China VI(b) are ~50% lower than those under China V. For heavy-duty diesel trucks (HDDTs), China VI(b) reduced the emissions of THC and NMHC by 48 and 11% respectively compared to China V (Table S1). This is achieved through unifying the fuel standards for gasoline and diesel vehicles, mandating the installation of gasoline particulate filters (GPF), and more detailed real driving emission (RDE) tests by China VI⁴⁰. According to our emission inventory, total vehicle-emitted THC decreased by 37.8% from 2019 to 2023 (Fig. S1). Previous bench tests also found that China VI has reduced organic vapor emissions by up to 87% compared with China V⁴¹.

In addition to vehicle emission, PN_{3-30} has several other sources in urban areas, including NPF, cooking and aviation^{12,42,43}. We targeted morning rush hours (6:00–9:00), and calculated emission rates of 3 to 30 nm particles (S_{3-30}) using aerosol general dynamic equation. By comparing S_{3-30} with the vehicle tracer measured by TDCIMS and vehicle factor extracted from PMF analysis, we employed it as a representative for PN emission rates attributed to vehicles ($S_{vehicle}$, see section “Verification of $S_{vehicle}$ quantification with online UFP composition measurements”). $S_{vehicle}$ showed a significant downward trend from 2019 to 2023 (Fig. 1b). The average $S_{vehicle}$ was $(2.27 \pm 1.87) \text{ cm}^{-3} \text{ s}^{-1}$ in 2019 and $(0.36 \pm 0.46) \text{ cm}^{-3} \text{ s}^{-1}$ in 2023, which has fallen by ~84%. The annual rates of decline were ~23%, ~33%, ~45% and ~45% for each year. The sharp decrease of $S_{vehicle}$ had a better consistency with that of PN_{3-30} than with PN of larger size.

To exclude the potential impact of meteorological conditions on $S_{vehicle}$ during long-term and short-term observation, we analyzed the interannual variations of temperature (T), relative humidity (RH), wind speed, wind direction, and surface boundary layer height (BLH) at the site. Overall, we found no significant interannual trends in T and RH. The diurnal variation pattern of BLH was relatively stable, with a smaller increase during morning rush hours in 2022, which may have led to a slightly weaker dilution effect in that year (Fig. S2). Light winds ($<1.5 \text{ m s}^{-1}$) dominated around the site, and we believe the detected particles were mainly from diffusion (Fig. S3). Furthermore, we performed meteorological normalization based on boosted regression trees⁴⁴ for $S_{vehicle}$, indicating that $S_{vehicle}$ after eliminating meteorological influences ($S_{vehicle_dw}$) maintained a consistent and significant downward trend (Fig. S4). Detailed discussion about the impact of meteorological conditions can be found in SI. In general, we consider the impact of meteorological conditions on this study to be acceptable. Additionally, Mann–Kendall tests were applied to total PN, $S_{vehicle}$ and $S_{vehicle_dw}$ to evaluate the significance of their decreasing trends. It is a nonparametric statistical method commonly used to test whether long-term data exhibit a monotonically increasing or decreasing trend. The Z value for PN, $S_{vehicle}$ and $S_{vehicle_dw}$ were -24.5 , -19.6 and -28.9 , respectively, stating a significant decreasing trend for all (Fig. S5).

For the seasonal variations, $S_{vehicle}$ was the highest in winter and the lowest in summer, (Fig. S6). The average $S_{vehicle}$ in winter, spring, summer and autumn were 3.84, 4.40, 1.19 and $1.74 \text{ cm}^{-3} \text{ s}^{-1}$ in 2019, and 0.54, 0.21, 0.17, and $0.36 \text{ cm}^{-3} \text{ s}^{-1}$ in 2023, respectively. The decreasing ratios from 2019 to 2023 were 86, 95, 86, and 79% in winter, spring, summer and autumn. Note that $S_{vehicle}$ in 2019 spring may be over-estimated due to the absence of data in April and May. The seasonal variation of $S_{vehicle}$ was caused by temperature-affected emission (especially during cold start stage), evaporation and condensation of semi-volatile components during atmospheric transport, as well as meteorological conditions. Firstly, vehicle-emitted particles are composed of both solid particles from direct emission and volatile particles from cold nucleation of organic vapors in exhaust gas, among which volatile particles can account for more than 70%⁷. At lower atmospheric temperature, the condensation effect becomes more pronounced, resulting in higher PN emission. Measurements conducted along a

major road in Toronto indicated that when ambient temperature decreased from $>20 \text{ }^\circ\text{C}$ to $<0 \text{ }^\circ\text{C}$, volatile ratio in particles increased from 85 to 94%⁶. In specific, higher PN emission during cold start stage was attributed to incomplete combustion and low efficiency of three-way catalysts^{45,46}, which can be more pronounced at low ambient temperature⁴⁷. Secondly, during the transport from emission sources to the sampling site, the semi-volatile components in the atmosphere and particles undergo redistribution. Dall’Osto⁴⁸ found particle shrinkage that the mode d_p decreased from ~20 nm at the roadside to 6 nm at the non-roadsite site in London. At low temperatures, semi-volatile components tend to condense, leading to particle growth during transport; at high temperatures, they tend to evaporate and result in particle shrinkage. According to our measurements, $S_{vehicle}$ in winter was ~2.2 times and ~1.5 times of that in summer in 2019 and 2023. Assuming the proportion of volatile components is 70%, with no evaporation occurring in winter and complete evaporation in summer, the $S_{vehicle}$ in winter should be 3.3 times that in summer, which is comparable to the measurement. Thirdly, the lower boundary layer in winter and spring than in summer and autumn could cause weaker dispersion conditions and higher ambient pollutant concentrations (Fig. S7).

The short-term reduction of UFPs due to restrictions in vehicles are also detected. During the sampling period, Beijing experienced two large-scale vehicle control periods, i.e., the 2020 COVID-19 lockdown (from Jan 24th to Feb 29th in 2020) and the 2022 Winter Olympics (from Jan 31st to Feb 20th in 2022). Sub-30 nm particles decreased significantly during the lockdown periods compared to normal days in winter of the same year. $S_{vehicle}$ decreased by 44% during COVID-19 lockdown and 56% during Winter Olympics. After meteorological normalization, $S_{vehicle_dw}$ decreased by 28% during COVID-19 lockdown and only by 8% during Winter Olympics (Fig. 1d). The lower decline rates of $S_{vehicle_dw}$ than those of $S_{vehicle}$ indicate that the short-term data before normalization are prone to being affected by extreme high values caused by meteorologically related sudden events, such as high-emission vehicles near the sampling site and their transport. On the contrary, above-30 nm particles increased during COVID-19 lockdown, consistency with the previously reported increased $PM_{2.5}$ attributed to unfavorable meteorological conditions^{49,50}. Figure S8 shows the daily variations of $S_{vehicle}$ and $S_{vehicle_dw}$, as well as city-averaged vehicle flow and NO_x concentrations during the lockdown periods. During the COVID-19 lockdown, the variation of $S_{vehicle}$ was well consistent with that of NO_x , while the variation of $S_{vehicle_dw}$ showed good consistency with vehicle flow.

The pervasive nature of UFPs attributed to vehicles in megacity

Not only at BUCT site, but among all of the four sites in Beijing we observed PN attributed to vehicle emissions. Figure 2b shows rise of PN_{10-30} at all of the sites in morning rush hours and Fig. 2c shows the appearance of Aitken mode particles due to morning-hour vehicle emission. The dataset includes the average of all sampling days at each site, respectively.

The BUCT site in 2019 showed the most distinguishable PN_{10-30} increase ($5.8 \times 10^3 \text{ cm}^{-3}$ absolute, or 134% ratio). Which could be because the BUCT site is close (~130 m) to the nearest traffic road and surrounded by another two traffic roads (550 m and 565 m away). The CRAES site was the closest to the nearest traffic road (~105 m), but the increase of PN_{10-30} was relatively small (~41% in the morning), likely because the site was a suburban area with lower intensity of traffic activity, and vehicle-attributed UFPs had already reduced significantly during the sampling time (2021) compared to earlier sampling time. PN_{10-30} increase at the THU site in 2016 was also significant and consistently observed at night. This may be caused by its earliest sampling year, when emissions from diesel vehicles had not yet been subject to sufficiently stringent controls, and large numbers of such vehicles enter Beijing’s urban areas via the 5th Ring Road (~1.7 km away) and Beijing–Xinjiang Expressway (~950 m away) during the night and early morning hours. Besides, the THU site is surrounded by several pathways within the campus. Traffic activity on these roads is typically less intense

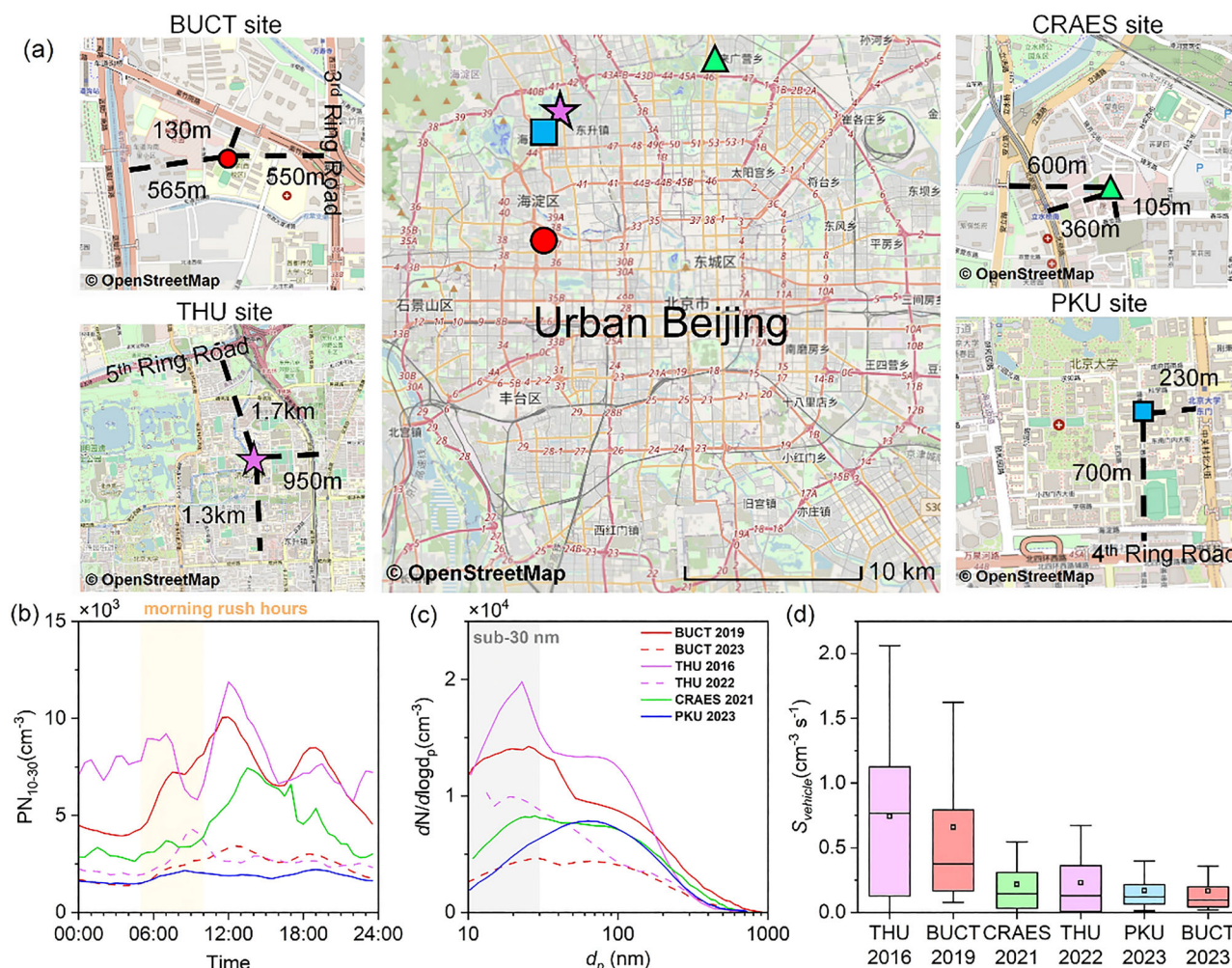


Fig. 2 | Locations of four sites with particle size distribution measurements and occurrence of vehicle-attributed particles at these sites in morning rush hours. Map of the sites and their surroundings (a), diurnal variations of PN of 10 to 30 nm (b), average particle number size distributions (c) and S_{vehicle} in morning rush hours (d). The red circle represents BUCT site, purple pentagram represents THU site, blue square represents PKU site and green triangle represents CRAES site. The particle

size ranges varied at different sites, and to ensure consistency, S_{vehicle} was calculated based on particles >10 nm. Data averaging periods: BUCT: 2019 and 2023; THU: Mar. 10th to Apr. 7th, 2016 and Dec. 7th to Feb. 28th, 2022; CRAES: Mar. 23rd to Apr. 30th, 2021; PKU: May. 1st, 2023 to Apr. 30th, 2024. The maps are from © OpenStreetMap (openstreetmap.org/copyright).

than on major roads, but may occasionally have a significant impact on observations due to their proximity to the sites.

S_{vehicle} for 10–30 nm particles were quantified at all sites and sorted by year (Fig. 2d), which showed a downward trend similar to long-term result at the BUCT site. To ensure comparability of data across sites, calculations here uniformly start from 10 nm, with data below 10 nm treated as missing values. As an advance of the study by Zhu et al.¹³, which found that vehicle-emitted particles became indistinguishable at >90 m away from a highway without busy traffic nearby, our analysis indicates that vehicle-source UFPs at urban sites may require longer distance to attenuate to background levels. Even for sites ~1 km away from the nearest road (e.g., THU site in 2016), the influence of vehicle emission can still be observed under high level background. This indicates that vehicle-source UFPs in urban area is affected by various factors, including but not limited to number of nearby roads and traffic flow that affect emission concentration, and surrounding buildings that affect dispersion condition.

In specific, although Fig. 2d shows a decreasing trend of S_{vehicle} at multiple sites, the exact decreasing ratio is hard to quantify due to the variations in traffic conditions, transport process (e.g., evaporation, dispersion, etc.), and sampling seasons for these observations. The long-term decline rate of S_{vehicle} is based on observations from a single site and it requires more evidence for citywide decline in

vehicle-attributed UFPs in Beijing. Nevertheless, this section demonstrates the pervasive nature of UFPs from vehicle emissions within complex urban environments, regardless of whether the receptor sites are immediately close to roads.

Verification of S_{vehicle} quantification with online UFP composition measurements

The representation of S_{3-30} during morning rush hours as vehicle-attributed PN emission rates (S_{vehicle}) was verified by the online UFP composition measurements.

Figure 3a–e shows a representative case covering 4 days from Nov 11th to 14th, 2019, at the BUCT site. Bursts of UFPs were frequently observed during morning and evening rush hours (Fig. 3a). The calculated PN emission rates (dS/dt) were the highest in the size range of sub-30 nm (Fig. 3b), indicating their intense sources. S_{3-30} peaked significantly during morning rush hours on Nov 11th, 12th, and 14th, and during evening rush hours on Nov 12th. The burst of sub-30 nm particles during morning rush hours can be initially judged as a typical characteristic of vehicle emission, since this period usually does not coincide with the occurrence of NPF. Although particles emitted from aviation activities may exhibit characteristics similar to those from vehicles⁴², the sites are located far from the airports (e.g., ~30 km and ~50 km for BUCT site) and within Beijing’s no-fly

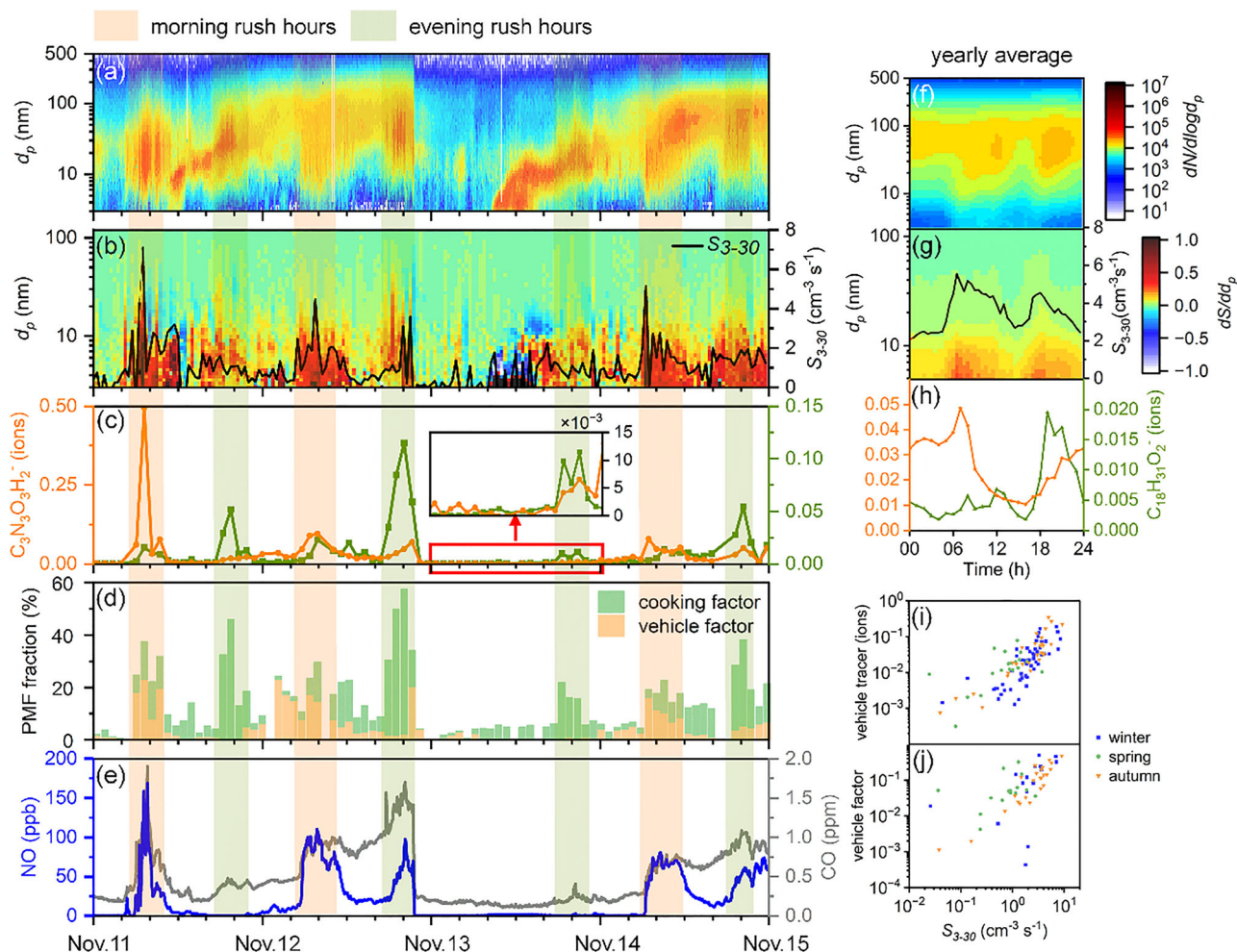


Fig. 3 | Representativeness of S_{vehicle} validated by UFP composition and PMF analysis. A typical period of emission during Nov. 11th and 14th, 2019 (a–e) and annual average situation (f–h). Correlation of S_{vehicle} with vehicle tracer measured by TDCIMS and vehicle factor quantified by PMF analysis (i–j). PNSD (a) and calculated particle emission rates at different diameters (dS/d_d) and accumulated

emission rates between 3–30 nm (S_{3-30}) (b), variation of signal intensities of traffic tracer ($\text{C}_3\text{N}_3\text{O}_3\text{H}_2^-$) and cooking tracer ($\text{C}_{18}\text{H}_{31}\text{O}_2^-$) (c), fractions of vehicle and cooking factors from PMF analysis (d) and variation of NO and CO at the same site (e). Orange rectangle represents morning rush hours and green rectangle represents evening rush hours.

zone in the urban area. Therefore, they are considered largely unaffected by aviation emissions. CO and NO are also major gaseous pollutants from vehicle exhaust, and their rises corresponded well to the peaks of S_{3-30} (Fig. 3e).

S_{3-30} during morning rush hours are highly related with the increase of vehicle-related UFP composition, while S_{3-30} during evening rush hours are more related with the increase of cooking-related UFP composition. Figure 3c shows the variations of a traffic tracer ($\text{C}_3\text{N}_3\text{O}_3\text{H}_2^-$) and a cooking tracer ($\text{C}_{18}\text{H}_{31}\text{O}_2^-$) measured by the TDCIMS in bulk UFP mode. $\text{C}_3\text{N}_3\text{O}_3\text{H}_2^-$ significantly peaked during morning rush hours and also increased relatively slightly during evening rush hours, while $\text{C}_{18}\text{H}_{31}\text{O}_2^-$ exhibited a distinct peak during the evening rush hours. Figure S9 listed the top 20 species most related to S_{3-30} respectively in morning and evening rush hours, proving the validity of the chosen tracers.

The PMF analysis further confirms the close relationships between S_{3-30} and vehicle/cooking factors. The identified five factors include a cooking-related factor, a vehicle related factor, a photooxidation-related factor and two aqueous/heterogeneous factors in winter, spring and autumn. And there are two photooxidation-related factors and one aqueous/heterogeneous factor in summer. The fraction of vehicle factor increased up to 20% during morning rush hours for overall UFP mass, and that of cooking factor achieved up to ~60% during evening rush hours. The higher contribution of

cooking to UFP mass is due to its larger particle sizes than vehicle emissions. In summary, sources of UFPs are relatively simpler in morning rush hours than that in evening rush hours, it is reasonable to consider S_{3-30} during morning rush hours as S_{vehicle} and representative of daily vehicle emission.

The strong correlation between morning rush hour S_{3-30} and vehicle emission can be expanded to the yearly average data (Fig. 3f–j), contains all non-NPF days). Generally, S_{3-30} exhibited a strong morning peak and a weaker evening peak. $\text{C}_3\text{N}_3\text{O}_3\text{H}_2^-$ reached its maximum value simultaneously with S_{3-30} in the morning, rapidly declined at noon, and rose again in the evening. $\text{C}_{18}\text{H}_{31}\text{O}_2^-$ exhibited slight peaks in the morning and midday, but a pronounced peak in the evening. This is also applicable in different seasons (Fig. S10). Summarizing all data from the year-round study, S_{vehicle} (S_{3-30} during morning rush hours) showed good correlation with both the vehicle tracer and PMF vehicle factor.

Driving factors of vehicle-attributed PN reduction

To assess the drivers of the pronounced reduction in vehicle-attributed PN concentrations, we developed PN emission inventories based on large-sample vehicle emission measurements and real-world vehicle usage data. Total vehicle PN emissions in Beijing decreased by 44%, from 4.4×10^{23} (1.2×10^{23} – 7.6×10^{23} , derived from the uncertainty range of PN emission factors in Fig. S11) # year⁻¹ in 2019 to 2.5×10^{23} (5.2×10^{22} – 4.4×10^{23}) #

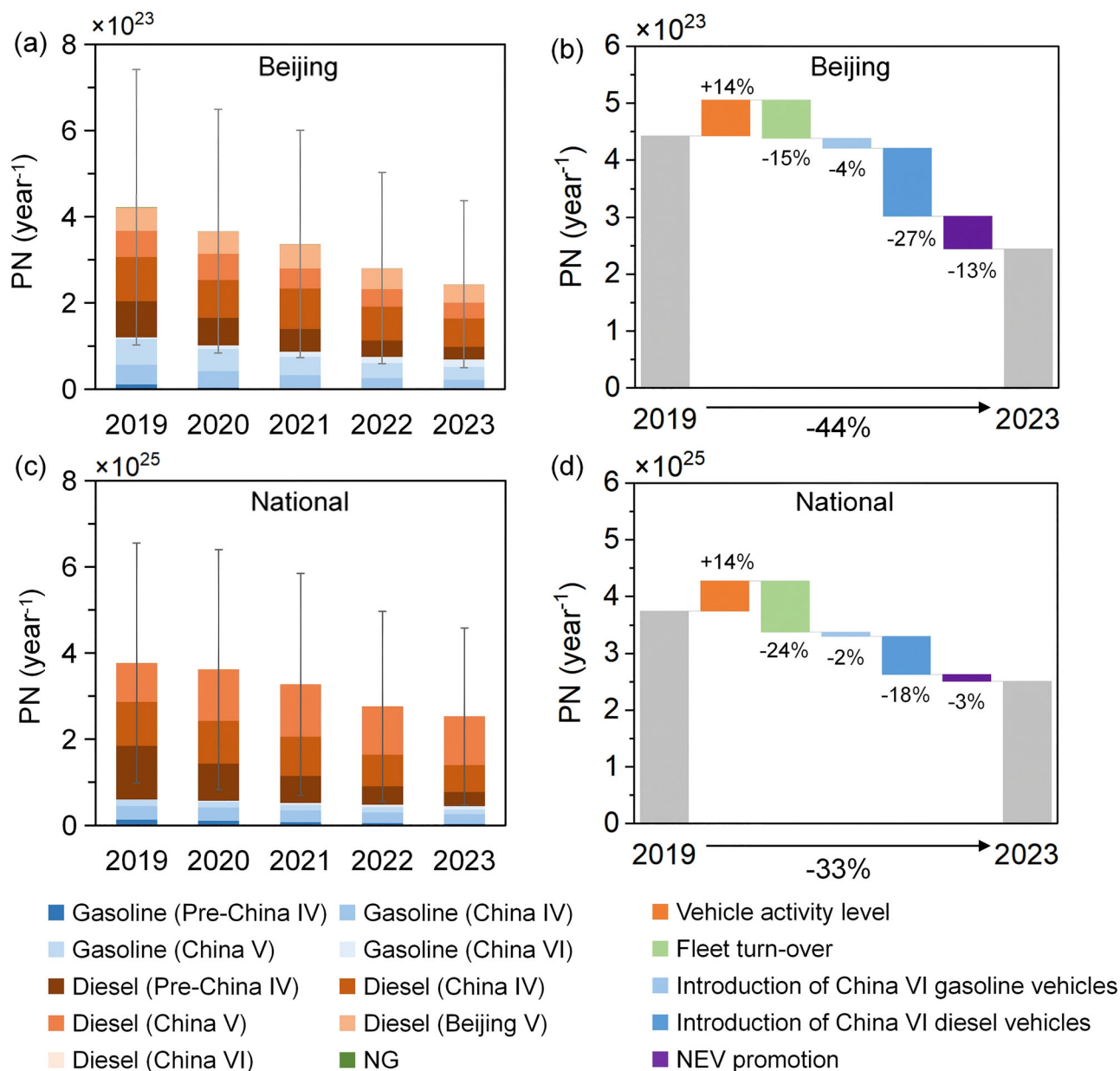


Fig. 4 | Vehicle PN emission inventory and driver analysis of emission changes from 2019 to 2023. PN emission inventories in Beijing (a) and nationwide (c) were classified by fuel type (gasoline, diesel and nature gas) and emission standards. Driver analysis in Beijing (b) and nationwide (d) included factors of vehicle activity level, fleet turn-over, introduction of China VI and new energy vehicle (NEV) promotion.

year⁻¹ in 2023 (Fig. 4a), exceeding the reduction rates of vehicle emitted NO_x (36%) and PM_{2.5} (33%). The nationwide PN reduction was less pronounced, with a reduction rate of 33% over the same period (Fig. 4c). Diesel vehicles accounted for 68–71% of total on-road PN emissions in Beijing, despite comprising only 5–7% of vehicle ownership and 14–20% of vehicle mileage in different years (Figs. S12 and S13), as fleet-average PN emission factors of diesel vehicles were 10–20 times higher than those of gasoline vehicles (Fig. S11). The contribution of diesel vehicles was even greater nationwide, accounting for 82–84% of total on-road PN emissions in China.

As shown in Fig. 4b, increased vehicle activity led to a 14% rise in total PN emissions in Beijing, whereas fleet turnover, the introduction of the China VI emission standard, and the promotion of new energy vehicles (NEVs) resulted in reductions of 15, 31, and 13%, respectively. Nationwide (Fig. 4d), increased vehicle activity contributed to a 14% rise in PN emissions, while fleet turnover, China VI implementation, and NEV adoption reduced emissions by 24, 20, and 3%, respectively.

The larger PN reduction in Beijing than nationwide was primarily driven by the earlier implementation of China VI and the accelerated adoption of electric vehicles. Beijing implemented the China VI emission standard in 2019, ahead of most other cities in 2021, mandating a PN limit of $6 \times 10^{11} \# \text{ km}^{-1}$ —one of the most stringent regulations globally. China VI diesel vehicles achieved more than 90% reduction in PN emissions compared with China V vehicles (Fig. S11). The implementation of China VI for diesel vehicles contributed the most to PN reductions (27%), and this fraction is only 18% for nationwide. NEV ownership in Beijing increased from 326,000 in 2019 to 773,000 in 2023, partly substituting for China VI gasoline vehicles due to purchase restrictions. This substitution contributed an additional 13% reduction in total PN emissions, much higher than the national reduction rate of 3%.

Compared to the observed reduction ratio of total atmospheric PN (−59%) in Beijing, the less reduction in emission inventory (−44%) may be because it did not include volatile particles, which were formed by

atmospheric condensation of organic vapors from vehicle exhaust. Volatile particles could account for a larger fraction of vehicle-attributed particles than solid particles^{6,7}. Additionally, the emission inventory considered particles of >23 nm, followed the regulations in China-VI. While S_{vehicle} focused on <30 nm ranges, the decrease of which is higher than larger particles.

Discussion

Despite the increased vehicle populations in Beijing, a sharp decrease of vehicle-attributed PN emission from 2019 to 2023 was observed from both field observation and emission inventory. Atmospheric PN_{3-30} in Beijing reduced by ~70%, far exceeding the decrease in $\text{PN}_{>30}$, $\text{PM}_{2.5}$, CO and NO_2 . This indicates that the involvement of PN in China VI benefits the reduction of smaller UFPs the most. Thanks to the advanced implementation of the new standards in Beijing, its vehicle-emitted PN reduction (~44%) is higher than other parts of China (~33%) and even higher than ever reported worldwide. Fleet turnover and proportional increase of NEV also contribute to the decrease in PN. Considering the current challenges in achieving deeper reduction in $\text{PM}_{2.5}$ in China, restrictions on PN might be easier to improve the health-oriented air quality. Whereas current standards and emission inventory focus on solid PN directly emitted by vehicles, while volatile PN, which may also contribute much to atmospheric UFPs and reduce with the control of THC emission, is not considered. A new standard might be required to include both solid and volatile PN in the future.

UFPs in urban areas have large spatial and temporal heterogeneity. At all the four urban sites, we observed significant PN increase and appearance of sub-30 nm particles in morning rush hours, even if the site was ~1 km far from main traffic roads. This indicates that vehicle-attributed UFPs can be ubiquitous in megacities, and their spatial variations deserve further analysis. There have been some UFP monitoring networks around the world, such as the global network conducted by NOAA⁵¹, and regional network in Germany⁵² and China^{53,54}. The aerosol dynamic method used in our study can be applied to assess the spatial distribution of UFPs affected by vehicles, as well as the long-term trends in UFP emission. We also suggested that spontaneous measurement of UFP compositions can help identify the sources attributed by vehicles.

Methods

Field sampling and quantification

The sampling site was on the fifth floor (~20 m high) of a teaching building at the west campus of Beijing University of Chemical Technology (BUCT, 39°94' N, 116°30' E)⁵⁵. It is surrounded by several traffic streets, commercial and residential buildings^{36,56}.

The PNSD measurement was conducted continuously from Jan 2019 to Dec 2023 using a customized particle size distribution system (PSD, 3 nm–10 μm) and a diethylene glycol scanning mobility particle spectrometer (DEG-SMPS, 1–7.5 nm) at time resolutions of 5 min^{57–59}. PSD consists of three instruments: a nano SMPS, a regular SMPS and an aerodynamic particle sizer (APS)⁶⁰. The instruments were calibrated 2–4 times a year. The sampling and sheath flow rates were calibrated by a soap film flowmeter (Sensidyne Gilian Gilibrator-2). The voltage of the differential mobility analyzer (DMA) was calibrated with a voltmeter. Mono-disperse Polystyrene Latex (PSL) with different sizes (50 nm to 2.5 μm) and aerosol generator were used to generate regular PNSD to calibrate the size accuracy. The counting efficiency of the condensation particle sizer (CPC) at the small size ends was calibrated using a Faraday cup electrometer⁶¹. The overlapping size ranges of different instruments are inverted to achieve a coincidence degree of >90%⁶⁰.

The UFP composition was measured from Oct 2019 to Aug 2021, obtained from a home-built TDCIMS operating in “bulk collection mode” with the time resolution of <1 h^{36,62}. The extremely low sampling efficiency for particles larger than 100 nm ensures that TDCIMS mainly measures particle compositions in the range of UFPs. It can measure a wide range of organics (CHO, CHON, CHOS, CHONS) and inorganics (sulfate, nitrate, etc.). Previous studies based on the TDCIMS have found tracers for traffic

emission in urban Beijing, i.e., $\text{C}_3\text{N}_3\text{O}_3\text{H}_2^-$ (assigned to deprotonated cyanuric acid), and tracers for cooking emission, i.e., $\text{C}_{18}\text{H}_{31}\text{O}_2^-$ (assigned to unsaturated fatty acids)³⁶. Meteorological data were also obtained. T, RH, wind speed and direction were measured by the meteorology stations (AWS310, Vaisala Inc., Finland). BLH was estimated by a three-step method by Eresmaa with backscattering coefficient profiles measured by a ceilometer (CL51, Vaisala Inc., Finland)⁵³. For other pollutants, NO_x and NO were measured at the BUCT site. In addition, continuous measurements of $\text{PM}_{2.5}$, CO, and NO_2 were obtained from the Haidian Wanliu site (40°00' N, 116°30' E), which is the closest national monitoring station to BUCT site.

The datasets also include PNSD at other three urban sites in Beijing. The measurements at THU site (40°00' N, 116°33' E) were on the fourth floor at the campus of Tsinghua University⁶⁴ from Mar to Apr 2016, and from Dec 2021 to Feb 2022. The measurements at the CRAES site (40°04' N, 116°41' E) were on the fifth floor of a building at the Chinese Research Academy of Environmental Sciences from Mar to Apr 2021. The measurements at PKU site (39°99' N, 116°31' E) were on the top of an eight-floor building (~30 m high) at the campus of Peking University⁶⁵ from May 2023 to Apr 2024. PKU site and THU site (2022) used a customized bipolar SMPS covering size range from 10 to 700 nm. This instrument has been used for long-term observations around China and demonstrated good consistency with conventional SMPS⁵⁴. The principle, performance and data quality were reported by Li et al.⁶⁶. CRAES site and THU site (2016) used PSD and DEG-SMPS mentioned above, covering size range from 1 nm to 10 μm . Among the three sites, CRAES are surrounded by residential communities and commercial districts, while THU and PKU sites are surrounded by teaching buildings and some restaurants.

NPF events were identified for all sampling data, and days were classified as NPF, non-NPF and undefined days. Criteria for NPF include (1) PN of sub-10 nm particles increased by more than threefold at midday, and (2) uninterrupted growth of mode d_p last for at least several hours. Days those nucleation events occurred but did not have significant “banana-shaped” growth were categorized as undefined days. Days without observed nucleation and growth were categorized as non-NPF days. Figure S14 summarizes annual distribution of NPF days.

Quantification of vehicle-attributed UFPs from observation

We used a population balance method based on the aerosol general dynamic equation to estimate the emission rates of UFPs. This method has been used to quantify the formation and growth rate of new particles^{64,67}, effect of transport on PNSD⁵⁹ and PN emission³⁷. The general form of the equation is shown in Eq. 1.

$$\frac{dN_{[i,j]}}{dt} = \left[GR_i n_i - GR_j n_j \right] + CoagSrc_{[i,j]} - CoagSnk_{[i,j]} + S_{[i,j]} + J_{[i,j]} \quad (1)$$

Where dN/dt ($\text{cm}^{-3} \text{s}^{-1}$) is the observed change rate of PN. The subscript i and j indicate lower and upper limits of particle diameters (d_p). GR (nm h^{-1}) represents the condensational growth rate of particles. n (cm^{-4}) is the number concentration density in certain size range. $CoagSrc$ and $CoagSnk$ represent sources and losses of PN due to coagulation at the observation site, further discussed in the supplementary information (SI). J ($\text{cm}^{-3} \text{s}^{-1}$) represents the secondary formation rates of new particles. S ($\text{cm}^{-3} \text{s}^{-1}$) represents the PN variations attributed to primary emissions. Notably, S does not purely represent the initial emission rate at the sources, but the influences of primary emission on the observation site. After the particles are emitted, they may go through volatilize, condensational growth, or coagulation during its transport from emission source to the observation site. As a result, S is a combination result of emission intensity and transport process. Figure S15 shows an example of S calculated from PNSD.

The uncertainty of using S to represent primary emission rates calculation also comes from: (1) Particle loss terms other than coagulation and condensation, such as dry deposition, are usually considered ignorable for

UFPs⁵⁹; (2) GR at different particle sizes is considered to be constant; (3) Neglecting J during non-NPF periods (e.g., morning and evening); (4) Potential changes in meteorological conditions may exert a non-negligible impact on the long-term trends and short-term abrupt changes. We adopted the open-source deweather R package to eliminate meteorological interference⁴⁴. This method was previously used to study the impact of the COVID-19 pandemic on air quality⁶⁸. Based on the boosted regression trees model, it incorporates meteorological variables (which are T, RH, wind speed, wind direction, and BLH in this study), temporal variables, and a trend term. The parameters of the model are set as: number of trees = 5; maximum tree depth = 200; learning rate = 0.1.

PMF analysis based on UFP chemical compositions

Furthermore, we applied Igor-based interface SoFi (solution finder, version 6.5) and ME-2 to run PMF analysis for organic compositions of UFPs measured by TDCIMS³⁶. The organic signal intensities in the m/z range of 100 to 300 were used as the input data matrix, since peaks of $m/z < 100$ mainly contain fragments and peaks of $m/z > 300$ exhibit low signal-to-noise ratios. In addition, peaks with more than 3% zero data points were not used. Finally, a total of 302 formulas were used for PMF analysis. The input error matrix for each peak was the sum of two parts: the square root of the signal intensity and the standard deviation when measuring zero air. Solutions with 3 to 10 factors were run sequentially. Based on the similarity of component profiles, time series, and diurnal variations within each factor, solutions with 5 factors were selected for each season.

Construction of vehicle PN emission inventories

The vehicle PN emission inventory in Beijing from 2019 to 2023 was calculated based on vehicle stock, vehicle activity level (VKT), and EF, using the following equation:

$$E_{PN,y} = VP_{v,y} \times X_{v,es,f,y} \times VKT_{v,y} \times EF_{PN,v,es,f,y} \quad (2)$$

where v represents the vehicle types (refer to Table S1 for detailed definitions); es represents the emission standard; f represents the fuel type; y represents the year, spanning from 2019 to 2023; $E_{PN,y}$ represents the total PN emissions from vehicles (unit: #/year); $VP_{v,y}$ represents the vehicle population by vehicle type in a specific year, obtained from the National Bureau of Statistics; $X_{v,es,f,y}$ represents the share of vehicle population by emission standard and fuel type for each vehicle type (expressed as a percentage); $VKT_{v,y}$ represents the annual vehicle kilometers traveled by vehicle type and year (unit: km), obtained from the National Vehicle Environmental Supervision Platform⁶⁹; $EF_{PN,v,es,f,y}$ represents the PN emission factors by vehicle type, emission standard, fuel type, and year (unit: particles/km), generated using the updated version of EMBEV model, the archetype of the on-road transportation chapter in the China National Emission Inventory Guidebook^{17,70,71}. The EMBEV model was developed based on large-sample vehicle emission measurements and real-world vehicle usage data. For example, the EF for LDGVs were derived from dynamometer tests of a fleet of 111 LDGVs in China⁴⁷, while those for HDDTs were obtained from portable emission measurement system (PEMS) tests of 66 HDDTs¹⁷.

The EF and error bars for LDGVs and HDDTs by emission standard are shown in Fig. S11. A Monte Carlo simulation was performed to quantify the uncertainty in emission estimates induced by emission factors. The simulation was repeated 100 times to estimate the emissions with a 95% confidence interval.

Data availability

The datasets generated and/or analyzed during the current study are not publicly available due to requirements imposed by the sampling site management and collaborating research institutions, but are available from the corresponding author on reasonable request.

Code availability

Data analysis was performed using MATLAB (Matrix Laboratory, Version R2023a, The MathWorks, Inc., Natick, MA, USA). The codes can be obtained from the corresponding author on reasonable request. The meteorological normalization was performed using deweather R package version 1.0.0, which is available on openair-project.github.io/deweather/.

Received: 16 October 2025; Accepted: 8 January 2026;

Published online: 23 January 2026

References

- Kwon, H.-S., Ryu, M. H. & Carlsten, C. Ultrafine particles: unique physicochemical properties relevant to health and disease. *Exp. Mol. Med.* **52**, 318–328 (2020).
- Ohlwein, S., Kappeler, R., Kutlar Joss, M., Künzli, N. & Hoffmann, B. Health effects of ultrafine particles: a systematic literature review update of epidemiological evidence. *Int. J. Public Health* **64**, 547–559 (2019).
- WHO. *WHO Global Air Quality Guidelines: Particulate Matter (PM_{2.5} and PM₁₀), Ozone, Nitrogen Dioxide, Sulfur Dioxide And Carbon Monoxide* (WHO, 2021).
- Kittelson, D. B., Watts, W. F. & Johnson, J. P. Nanoparticle emissions on Minnesota highways. *Atmos. Environ.* **38**, 9–19 (2004).
- Straaten, A., Nguyen, M.-H. & Weber, S. Real world ultrafine particle emission factors for road-traffic derived from multi-year urban flux measurements using eddy covariance. *Environ. Sci. Atmos.* **3**, 1439–1452 (2023).
- Wang, J. M. et al. Real-world emission of particles from vehicles: volatility and the effects of ambient temperature. *Environ. Sci. Technol.* **51**, 4081–4090 (2017).
- Li, X. et al. Size distribution of vehicle emitted primary particles measured in a traffic tunnel. *Atmos. Environ.* **191**, 9–18 (2018).
- Saha, P. K. et al. Quantifying high-resolution spatial variations and local source impacts of urban ultrafine particle concentrations. *Sci. Total Environ.* **655**, 473–481 (2019).
- Meier, R. et al. Ambient ultrafine particle levels at residential and reference sites in urban and rural Switzerland. *Environ. Sci. Technol.* **49**, 2709–2715 (2015).
- Xiang, S., Hu, Z., Zhai, W., Wen, D. & Noll, K. E. Concentration of ultrafine particles near roadways in an urban area in Chicago, Illinois. *Aerosol Air Qual. Res.* **18**, 895–903 (2018).
- Giechaskiel, B., Vanhanen, J., Väkevä, M. & Martini, G. Investigation of vehicle exhaust sub-23 nm particle emissions. *Aerosol Sci. Technol.* **51**, 626–641 (2017).
- Zhang, F. et al. Real world particle size distribution from vehicle fleet and implication on emission control. *npj Clean Air* **1**, 8 (2025).
- Zhu, Y., Hinds, W. C., Kim, S. & Sioutas, C. Concentration and size distribution of ultrafine particles near a major highway. *J. Air Waste Manag. Assoc.* **52**, 1032–1042 (2002).
- Zhu, Y., Hinds, W. C., Kim, S., Shen, S. & Sioutas, C. Study of ultrafine particles near a major highway with heavy-duty diesel traffic. *Atmos. Environ.* **36**, 4323–4335 (2002).
- Karner, A. A., Eisinger, D. S. & Niemeier, D. A. Near-roadway air quality: synthesizing the findings from real-world data. *Environ. Sci. Technol.* **44**, 5334–5344 (2010).
- National Bureau of Statistics of the People's Republic of China. Statistical Communiqué of the People's Republic of China on the 2024 National Economic and Social Development. Retrieved from https://www.stats.gov.cn/sj/zxfb/202502/t20250228_1958817.html (2025).
- Wen, Y. et al. Updating on-road vehicle emissions for China: spatial patterns, temporal trends, and mitigation drivers. *Environ. Sci. Technol.* **57**, 14299–14309 (2023).
- Zhang, S., Fu, M., Zhang, H., Yin, H. & Ding, Y. Emission control status and future perspectives of diesel trucks in China. *J. Environ. Sci.* **148**, 702–713 (2023).

19. Feng, R., Hu, X., Li, G., Sun, Z. & Deng, B. A comparative investigation between particle oxidation catalyst (POC) and diesel particulate filter (DPF) coupling aftertreatment system on emission reduction of a non-road diesel engine. *Ecotoxicol. Environ. Saf.* **238**, 113576–113576 (2022).
20. Zhang, Z., Dong, R., Lan, G., Yuan, T. & Tan, D. Diesel particulate filter regeneration mechanism of modern automobile engines and methods of reducing PM emissions: a review. *Environ. Sci. Pollut. Res.* **30**, 39338–39376 (2023).
21. Li, D. et al. Exploring ultrafine particle emission characteristics from in-use light-duty diesel trucks in China using a portable measurement system. *Environ. Res.* **263**, 120234–120234 (2024).
22. He, L. et al. Tailpipe emissions and fuel consumption of a heavy-duty diesel vehicle using palm oil biodiesel blended fuels. *Sci. Total Environ.* **955**, 177048–177048 (2024).
23. IEA, Global EV Outlook 2024, IEA, Paris <https://www.iea.org/reports/global-ev-outlook-2024>, Licence: CC BY 4.0 (2024).
24. Li, B. et al. Real-world identification of high-emitting vehicles based on near-road sensor measurement. *Front. Environ. Sci. Eng.* **19**, 63 (2025).
25. Shen, Y. et al. Evaluation of a cost-effective roadside sensor platform for identifying high emitters. *Sci. Total Environ.* **816**, 151609–151609 (2021).
26. Lähde, T. et al. Solid particle number emissions of 56 light-duty Euro 5 and Euro 6 vehicles. *J. Aerosol Sci.* **159**, 105873–105873 (2021).
27. Sun, J. et al. Decreasing trends of particle number and black carbon mass concentrations at 16 observational sites in Germany from 2009 to 2018. *Atmos. Chem. Phys.* **20**, 7049–7068 (2020).
28. Garcia-Marlès, M. et al. Inter-annual trends of ultrafine particles in urban Europe. *Environ. Int.* **185**, 108510–108510 (2024).
29. Presto, A. A., Saha, P. K. & Robinson, A. L. Past, present, and future of ultrafine particle exposures in North America. *Atmos. Environ. X* **10**, 100109–100109 (2021).
30. Kulmala, M. et al. Formation and growth rates of ultrafine atmospheric particles: a review of observations. *J. Aerosol Sci.* **35**, 143–176 (2004).
31. Lonati, G., Crippa, M., Gianelle, V. & Van Dingenen, R. Daily patterns of the multi-modal structure of the particle number size distribution in Milan, Italy. *Atmos. Environ.* **45**, 2434–2442 (2011).
32. Xue, W., Xue, J., Mousavi, A., Sioutas, C. & Kleeman, M. J. Positive matrix factorization of ultrafine particle mass (PM_{0.1}) at three sites in California. *Sci. Total Environ.* **715**, 136902 (2020).
33. Leoni, C. et al. Source apportionment of aerosol particles at a European air pollution hot spot using particle number size distributions and chemical composition. *Environ. Pollut.* **234**, 145–154 (2018).
34. Cai, J. et al. Size-segregated particle number and mass concentrations from different emission sources in urban Beijing. *Atmos. Chem. Phys.* **20**, 12721–12740 (2020).
35. Ge, Y. et al. High spatial resolution land-use regression model for urban ultrafine particle exposure assessment in Shanghai, China. *Sci. Total Environ.* **816**, 151633–151633 (2021).
36. Li, X. et al. Seasonal variations in composition and sources of atmospheric ultrafine particles in urban Beijing based on near-continuous measurements. *Atmos. Chem. Phys.* **23**, 14801–14812 (2023).
37. Kontkanen, J. et al. Size-resolved particle number emissions in Beijing determined from measured particle size distributions. *Atmos. Chem. Phys.* **20**, 11329–11348 (2020).
38. Smith, J. N., Moore, K. F., McMurry, P. H. & Eisele, F. L. Atmospheric measurements of sub-20 nm diameter particle chemical composition by thermal desorption chemical ionization mass spectrometry. *Aerosol Sci. Technol.* **38**, 100–110 (2004).
39. Damayanti, S., Harrison, R. M., Pope, F. & Beddows, D. C. S. Limited impact of diesel particle filters on road traffic emissions of ultrafine particles. *Environ. Int.* **174**, 107888 (2023).
40. Yan, F. & Zhao, H. Research on the impacts of GPF on RDE emission behaviors. *E3S Web Conf.* **522**, 01005 (2024).
41. Kong, L. et al. Speciated volatile organic compounds and hydroxyl radical reactivity characteristics of evaporation emissions from China VI and China V in-use light-duty gasoline vehicles. *Atmos. Chem. Phys.* **25**, 13311–13326 (2025).
42. Austin, E. et al. Distinct ultrafine particle profiles associated with aircraft and roadway traffic. *Environ. Sci. Technol.* **55**, 2847–2858 (2021).
43. Sun, J. et al. Measurement report: contribution of atmospheric new particle formation to ultrafine particle concentration, cloud condensation nuclei, and radiative forcing – results from 5-year observations in central Europe. *Atmos. Chem. Phys.* **24**, 10667–10687 (2024).
44. Carslaw, D. & Davison, J. deweather: remove the influence of weather on air quality data. R package version 1.0.0. <https://openair-project.github.io/deweather/> (2025).
45. Gramigni, F., Selleri, T., Nova, I. & Tronconi, E. Catalyst systems for selective catalytic reduction + NO_x trapping: from fundamental understanding of the standard SCR reaction to practical applications for lean exhaust after-treatment. *React. Chem. Eng.* **4**, 1165–1178 (2019).
46. Klems, J. P., Pennington, M. R., Zordan, C. A., McFadden, L. & Johnston, M. V. Apportionment of motor vehicle emissions from fast changes in number concentration and chemical composition of ultrafine particles near a roadway intersection. *Environ. Sci. Technol.* **45**, 5637–5643 (2011).
47. Wen, Y. et al. Characterizing start emissions of gasoline vehicles and the seasonal, diurnal and spatial variabilities in China. *Atmos. Environ.* **245**, 118040 (2021).
48. Dall’Osto, M. et al. Remarkable dynamics of nanoparticles in the urban atmosphere. *Atmos. Chem. Phys.* **11**, 6623–6637 (2011).
49. Le, T. et al. Unexpected air pollution with marked emission reductions during the COVID-19 outbreak in China. *Science* **369**, 702–706 (2020).
50. Sun, Y. et al. A chemical cocktail during the COVID-19 outbreak in Beijing, China: Insights from six-year aerosol particle composition measurements during the Chinese New Year holiday. *Sci. Total Environ.* **742**, 140739 (2020).
51. Andrews, E. et al. Overview of the NOAA/ESRL federated aerosol network. *Bull. Am. Meteor. Soc.* **100**, 123–135 (2018).
52. Birmili, W. et al. Long-term observations of tropospheric particle number size distributions and equivalent black carbon mass concentrations in the German Ultrafine Aerosol Network (GUAN). *Earth Syst. Sci. Data* **8**, 355–382 (2016).
53. Wu, J. et al. Characterizing airborne nanoparticles in six Chinese cities based on their interactions with natural air ions. *Environ. Sci. Nano* **12**, 1138–1149 (2025).
54. Li, Y. et al. A bipolar SMPS network for measuring atmospheric aerosols using natural air ions. *Atmos. Environ.* **325**, 120462 (2024).
55. Liu, Y. et al. Continuous and comprehensive atmospheric observations in Beijing: a station to understand the complex urban atmospheric environment. *Big Earth Data* **4**, 295–321 (2020).
56. Deng, C. et al. Measurement report: size distributions of urban aerosols down to 1 nm from long-term measurements. *Atmos. Chem. Phys.* **22**, 13569–13580 (2022).
57. Cai, R. et al. Aerosol surface area concentration: a governing factor in new particle formation in Beijing. *Atmos. Chem. Phys.* **17**, 12327–12340 (2017).
58. Deng, C. et al. Seasonal characteristics of new particle formation and growth in Urban Beijing. *Environ. Sci. Technol.* **54**, 8547–8557 (2020).
59. Abbatt, J. P. D. et al. Overview paper: new insights into aerosol and climate in the Arctic. *Atmos. Chem. Phys.* **19**, 2527–2560 (2019).
60. Liu, J., Jiang, J., Zhang, Q., Deng, J. & Hao, J. A spectrometer for measuring particle size distributions in the range of 3 nm to 10 μm. *Front. Environ. Sci. Eng.* **10**, 63–72 (2014).

61. Intra, P. & Tippayawong, N. Performance evaluation of an electrometer system for ion and aerosol charge measurements. *Korean J. Chem. Eng.* **28**, 527–530 (2011).
62. Li, X. et al. Composition of ultrafine particles in urban Beijing: measurement using a thermal desorption chemical ionization mass spectrometer. *Environ. Sci. Technol.* **55**, 2859–2868 (2021).
63. Eresmaa, N. et al. A three-step method for estimating the mixing height using ceilometer data from the Helsinki testbed. *J. Appl. Meteorol. Climatol.* **51**, 2172–2187 (2012).
64. Cai, R. & Jiang, J. A new balance formula to estimate new particle formation rate: reevaluating the effect of coagulation scavenging. *Atmos. Chem. Phys.* **17**, 12659–12675 (2017).
65. Cheng, X. et al. Secondary production of gaseous nitrated phenols in polluted urban environments. *Environ. Sci. Technol.* **55**, 4410–4419 (2021).
66. Li, Y., Chen, X. & Jiang, J. Measuring size distributions of atmospheric aerosols using natural air ions. *Aerosol Sci. Technol.* **56**, 655–664 (2022).
67. Kuang, C. et al. Size and time-resolved growth rate measurements of 1 to 5 nm freshly formed atmospheric nuclei. *Atmos. Chem. Phys.* **12**, 3573–3589 (2012).
68. Ceballos-Santos, S. et al. Meteorological normalisation using boosted regression trees to estimate the impact of COVID-19 restrictions on air quality levels. *IJERPH* **18**, 13347 (2021).
69. Ma, D. et al. The characteristics of light-duty passenger vehicle mileage and impact analysis in China from a big data perspective. *Atmosphere* **13**, 1984 (2022).
70. Zhang, S. et al. Historic and future trends of vehicle emissions in Beijing, 1998–2020: a policy assessment for the most stringent vehicle emission control program in China. *Atmos. Environ.* **89**, 216–229 (2014).
71. Wu, Y. et al. On-road vehicle emissions and their control in China: a review and outlook. *Sci. Total. Environ.* **574**, 332–349 (2017).

Acknowledgements

Financial support from the National Natural Science Foundation of China (22376166 and 22406024), the Fundamental Research Funds for the Central Universities (grant number 2042025kf0047), the special fund of State Environmental Protection Key Laboratory of Formation and Prevention of Urban Air Pollution Complex (SEPAir-2024080214), and Natural Science Foundation of Wuhan (2024040801020229) is acknowledged.

Author contributions

X.L., J.J., H.Q.W., and Y.W. designed the study. H.Q.W. and Y.W. participated in data analysis and wrote the original draft. J.W. and R.C. contributed to methodology. J.W., Y.S., C.D., Y.Y.L., Y.R.L., H.W., M.Z., and Y.C.L. contributed to data collection. C.Y., J.G., and S.Z. contributed to data curation and validity. D.H., H.C., M.K., F.M., J.S., and J.H. contributed to review and editing. All authors approved the final version of the manuscript.

Competing interests

The authors declare no competing interests.

Additional information

Supplementary information The online version contains supplementary material available at <https://doi.org/10.1038/s41612-026-01327-6>.

Correspondence and requests for materials should be addressed to Xiaoxiao Li or Jingkun Jiang.

Reprints and permissions information is available at <http://www.nature.com/reprints>

Publisher's note Springer Nature remains neutral with regard to jurisdictional claims in published maps and institutional affiliations.

Open Access This article is licensed under a Creative Commons Attribution-NonCommercial-NoDerivatives 4.0 International License, which permits any non-commercial use, sharing, distribution and reproduction in any medium or format, as long as you give appropriate credit to the original author(s) and the source, provide a link to the Creative Commons licence, and indicate if you modified the licensed material. You do not have permission under this licence to share adapted material derived from this article or parts of it. The images or other third party material in this article are included in the article's Creative Commons licence, unless indicated otherwise in a credit line to the material. If material is not included in the article's Creative Commons licence and your intended use is not permitted by statutory regulation or exceeds the permitted use, you will need to obtain permission directly from the copyright holder. To view a copy of this licence, visit <http://creativecommons.org/licenses/by-nc-nd/4.0/>.

© The Author(s) 2026

¹School of Resource and Environmental Sciences, Wuhan University, Wuhan, China. ²School of Environment, Beijing Normal University, Beijing, China. ³State Key Joint Laboratory of Environment Simulation and Pollution Control, School of Environment, Tsinghua University, Beijing, China. ⁴Shanghai Key Laboratory of Atmospheric Particle Pollution and Prevention (LAP3), Department of Environmental Science & Engineering, Fudan University, Shanghai, China. ⁵Chinese Research Academy of Environmental Sciences, Beijing, China. ⁶State Environmental Protection Key Laboratory of Formation and Prevention of Urban Air Pollution Complex, Shanghai Academy of Environmental Sciences, Shanghai, China. ⁷Joint International Research Laboratory of Atmospheric and Earth System Sciences, School of Atmospheric Sciences, Nanjing University, Nanjing, China. ⁸State Key Joint Laboratory of Environment Simulation and Pollution Control, College of Environmental Sciences and Engineering, Peking University, Beijing, China. ⁹Aerosol and Haze Laboratory, Beijing Advanced Innovation Center for Soft Matter Science and Engineering, Beijing University of Chemical Technology, Beijing, China. ¹⁰Institute for Atmospheric and Earth System Research/Physics, Faculty of Science, University of Helsinki, Helsinki, Finland. ¹¹School of Remote Sensing and Information Engineering, Wuhan University, Wuhan, China. ¹²Chemistry Department, University of California, Irvine, CA, USA. ¹³These authors contributed equally: Haoqian Wang, Yifan Wen. ✉ e-mail: lixiaoxiao@whu.edu.cn; jiangjk@tsinghua.edu.cn